The manuscript has been accepted for publication in Composites Part A

Deducing the R-curve for Trans-laminar Fracture from a Virtual Over-height Compact Tension (OCT) Test

Xiaodong Xu*, Michael R. Wisnom and Stephen R. Hallett

Bristol Composites Institute (ACCIS), University of Bristol, University Walk, Bristol BS8 1TR, United Kingdom

Abstract

The R-curve for Mode I trans-laminar fracture energy in quasi-isotropic IM7/8552 carbon/epoxy laminates is here deduced numerically from a virtual Over-height Compact Tension (OCT) test. A High-fidelity Finite Element Method (Hi-FEM) using the explicit Finite Element (FE) software LS-Dyna was adopted. Cohesive interface elements and a Weibull fibre failure criterion were used to predict failure. The input parameters for the Hi-FEM were measured from independent characterisation tests. OCT specimens were tested to verify the Hi-FEM results with good agreement. The R-curve effect is postulated to be caused by the growth of the height of the Fracture Process Zone (FPZ) with crack length. Hi-FEM can be used to better understand Mode I trans-laminar fracture toughness tests and generate fracture properties such as damage heights and R-curves for future structural scale models.

Keywords: A. Laminates; B. Fracture; B. Fracture Toughness; C. Finite Element Analysis (FEA); R-curve

* Corresponding author. Tel.: +44 (0)117 33 15796.
E-mail address: xiaodong.xu@bristol.ac.uk (X. Xu)

1. Introduction

The existence of a fracture resistance curve, or R-curve, has profound implications on the failure prediction of composite structures. The R-curve describes the relationship between the fracture resistance R and the crack increment Δa. For metallic materials, the fracture resistance R is not a constant value, but increases during crack propagation [1]. For composite materials, the question of R-curves is still subject to debate. On the one hand, R-curves have been reported for Mode I trans-laminar fracture e.g. in coupon tests [2-7] and observed in full-scale composite structural tests [8]. On the other hand, many existing approaches for modelling Mode I trans-laminar fracture [9-12] do not directly address R-curves and assume a constant Mode I trans-laminar fracture toughness value during fracture propagation.

Efforts have been made to predict trans-laminar fracture in composite laminates for Fracture Process Zone (FPZ) development [13, 14], and fracture propagation [15-17]. However, they have not addressed R-curves. Although some other methods [2-4, 6, 7] have considered R-curves, they were mainly for cross-ply laminates. Efforts have also been made to establish R-curves for Mode I trans-laminar fracture in Quasi-isotropic (QI) laminates in the literature such as for $[90/0/\pm45]_{3s}$ IM7/8552 material in Ref. [5]. Catalanotti et al. [18] also applied their method to QI CP-T700/ACE Non-Crimp Fabrics. The approaches [6, 10, 11, 18] to determine trans-laminar fracture toughness either rely on inputs from modelled notched tests [10, 11], or the results from separate sets of scaled notched tensile tests [18]. The numerical prediction of R-curves for QI laminates without input parameters from the modelled fracture tests has not been reported before.

To determine the R-curves for composites, the Mode I trans-laminar fracture energy G_C (equal to R) and crack increment Δa need to be measured. Laffan et al. [19] reviewed the existing test methods for Mode I trans-laminar fracture toughness of composites. The Centre-notched Tension (CNT) [5, 20] and Edge-notched Tension (ENT) [18, 21, 22] configurations can be used to determine Mode I trans-laminar fracture toughness. One characteristic of these configurations is that the fracture propagation is unstable, so a single set of tests is not sufficient to generate the full R-curve and multiple sets of scaled notched specimens are needed [18]. An alternative geometry to generate stable fracture in a single test is the Compact Tension configuration, for example following the ASTM E399 standard [23], originally for metals. Compact Tension specimens have been widely used for the determination of R-curves for Mode I trans-laminar fracture in composites [3, 5, 6]. One limitation of that configuration is that the specimen may suffer from compressive failure at the top, bottom and rear ends. An Over-height Compact Tension (OCT) test was therefore developed to reduce the potential compressive failures [24]. The OCT configuration has been used in numerous studies [10, 25, 26].

The definition and measurement of crack increments, Δa, in the above fracture tests has proven challenging. For example, Pinho et al. [2] relied on the optically measured crack length at the specimen surface, while others turned to the Digital Image Correlation (DIC) technique [4, 10]. These optical and DIC measurements are limited to the specimen surfaces, so assumptions must be made to relate the surface measurements to the internal fracture. X-ray Computed Tomography (CT) has been adopted to better understand the internal damage states and fracture [26]. However, multiple interrupted tests are needed for the crack length measurements. Some FE methods for estimating

the crack increment in Mode I trans-laminar fracture tests have been developed. For example, a Modified Compliance Calibration (MCC) method was developed by Laffan et al. [3]. Compact Tension specimens with several pre-machined notch lengths were tested to establish the compliance vs. crack length relationship. Then a linear elastic FE analysis was used to back-calculate the crack length at any measured compliance during fracture testing. However, the linear elastic FE analysis does not account for the material non-linearity due to the complex behaviour in the Fracture Process Zone (FPZ). Bergan et al. [6] implemented their characterised cohesive law in an FE analysis, in which the crack increment was calculated numerically as the distance from the initial notch tip to the first undamaged element. DIC was used to check out-of-plane deformation and CT scans were used to check damage development, but they were not adopted for crack length measurements in Ref. [6].

Also, the definition of what constitutes a crack is problematic, e.g. if some plies are fractured and some are intact. In the definition of crack length for the determination of R-curves that consider an FPZ [4-6], the FPZ was added to the crack length. In the current study, this crack length is referred to as the effective crack length a_{eff}. This is a common procedure for the determination of Mode I trans-laminar fracture toughness for composites [8, 27]. At the end of the paper an alternative definition of crack length, by distinguishing between the FPZ development and fracture propagation [26], is discussed.

In this paper, a High-fidelity Finite Element Method (Hi-FEM) is developed to numerically predict the R-curve for Mode I trans-laminar fracture energy in QI laminates without any input parameters from the fracture tests modelled. Initially, the effective R-curve for Mode I trans-laminar fracture was determined by using a

Numerical Compliance Calibration (NCC) method from the predicted fracture response and the effective crack increments Δa_{eff}. Hi-FEM results were successfully verified by comparison with scaled-down OCT tests. It is shown that the damage height grows during fracture propagation and it is postulated that this causes the R-curve. An alternative definition of R-curves is also discussed later, and the adjusted true R-curve is consistent with other G_C values reported in the literature. The current paper helps to clarify the definition of the R-curve for quasi-isotropic laminates and its key elements such as crack length, size of the FPZ and damage height.

2. Virtual Over-height Compact Tension (OCT) test

A Hi-fidelity Finite Element Method (Hi-FEM) has been developed to predict the Mode I trans-laminar fracture in composite laminates using the explicit FE software LS-Dyna. The Hi-FEM combines the FEM methods from [13, 17], with potential delaminations and multiple split paths explicitly modelled using cohesive interface elements, together with an automated meshing technique [28]. Previously, the focus was on delamination dominated failure in QI laminates with blocked plies [17] and the FPZ development including splitting, delamination and local fibre breakage with dispersed plies [13]. Now, going beyond the FPZ development, the R-curve for Mode I trans-laminar fracture energy in QI laminates with dispersed plies is predicted.

A scaled-down version [26] of the standard OCT specimen [24] was modelled in the present study. This configuration was chosen because it was found to be able to generate stable Mode I trans-laminar fracture propagation. The scaled-down OCT specimen also reduces the computational cost. The dimensions of the scaled-down OCT specimen and the test fixture assembly are shown in Figure 1.

Hexcel's HexPly® IM7/8552 carbon/epoxy UD pre-preg was used in the current study. The stacking sequence of $[90/45/0/-45]_{4s}$ was used, with 0° being the loading direction. The nominal ply thickness is 0.125 mm, so the nominal specimen thickness is 4 mm, which is close to the actual specimen thickness.

Following the method introduced in Ref. [28], a unit-cell mesh was created, which can accommodate potential splitting of different orientations as shown in Figure 2. The in-plane refined mesh is the same in each lamina with a minimum size of 0.125 mm. It covers an area of 26.5 mm by 20 mm, from the mid width near the crack tip to the rear end of the model. The intention is to capture the progressive damage evolution and fracture propagation within the refined mesh. The mesh was then transitioned to a coarser mesh elsewhere. The width of the notch was kept at 1 mm, the same as that in the experiments. Instead of using a semi-circular radius like in the scaled-down OCT specimen, a 90° triangular notch tip was modelled to adapt to the unit cell based in-plane mesh pattern. It has been demonstrated experimentally that so long as the radius is no larger than 0.5 mm for quasi-isotropic laminates [5], the measured trans-laminar fracture energy is not sensitive to the local notch tip radius. It has also been demonstrated numerically that the 90° triangular notch tip is sufficient to simulate the FPZ development [13]. This results in a sharper notch tip than that in the experiments, causing early fibre breakage at the notch tip in the Hi-FEM model. This means that the determined apparent trans-laminar fracture energy at the first failure is not directly comparable with that obtained experimentally. However, after the first fibre breakage, the crack propagation is no longer influenced by the initial crack tip in the Hi-FEM model since it initiates from the newly predicted crack front. Therefore, the determined trans-laminar fracture energy after the first fibre failure is representative. It has already

been demonstrated numerically in another centre-notched configuration that with the same 90° triangular notch tip, the results were not sensitive to the minimum mesh size of no larger than 0.2 mm [13]. These justify the current mesh size and the shape of the notch tip in the Hi-FEM model.

The in-plane refined mesh was partitioned, and cohesive interface elements were inserted in between the adjacent parts to simulate potential intra-laminar splitting. According to Ref. [13], it is crucial to simulate multiple 0° splits and delaminations ahead of the crack tip to capture the progressive damage growth. In the current study, multiple potential split paths were pre-defined in all plies (0°, 90° and ±45°) as per their ply orientations, at a constant spacing of 0.5 mm, as shown in Figure 3. It has been shown that so long as the distance between splits in the 0° plies is 1 mm or less, the results are not sensitive to the split spacing [13]. The laminae were then connected with cohesive interface elements to simulate delamination. Further to the previous study, the aim here is to capture the entire complex failure process throughout fracture propagation via Hi-FEM, so pre-defined multiple potential split paths were also extended beyond the expected initial FPZ and across the model half width.

A mixed-mode traction-displacement relationship for cohesive interface elements has been adopted based on the user-defined material subroutine developed by Jiang et al. [29], as illustrated in Figure 4. The cohesive interface elements linearly soften when the initiation criterion is met. When the propagation (full debonding) criterion is satisfied, the cohesive interface elements are deleted to simulate the discrete damage.

A fibre failure criterion based on Weibull theory [17, 30] has been implemented in the Hi-FEM model. The probability of failure is defined as a function of both the volume and the stress through the Weibull integration in Equation 1, which is checked at each

time step in the Hi-FEM model. When Equation 1 is satisfied, the element with the maximum fibre-direction stress is deleted, and the stress is redistributed. The fibre failure criterion is checked again at the next time step and the element deletion process repeats to simulate the progressive fracture. Contact is not enforced along the crack path after elements are deleted, which is found not to affect the predicted load-Pin Opening Displacement (POD) curve significantly over a POD of around 1.4 mm as element penetration is only present in the unloaded region.

$$\sum_{i=1}^{\text{Total Number of Elements}} V_i (\sigma_i / \sigma_{\text{unit}})^m = 1 \quad (1)$$

where σ_i is the elemental stress, V_i is the volume of the element i, σ_{unit} = 3131 MPa is the tensile strength of a unit volume of material and m = 41 is the Weibull modulus [31].

Half the thickness of the scaled-down OCT specimen was modelled with 1 continuum element per ply through the model thickness, with symmetry boundary conditions applied at the mid-plane. A -160°C temperature drop was applied before mechanical loading, to generate the thermal residual stresses formed during cooling down after curing. The thermal step slightly affects the results. Without consideration of the thermal residual stresses, the predicted fracture response is slightly less tough. This could be due to the lack of compressive thermal residual stresses in the fibre direction. Uniform displacements were then applied in opposite directions to the nodes at the positions of the contact points of the two loading pins. The material properties for the Hi-FEM model are listed in Table 1 [31]. The penalty stiffness used for the cohesive interface elements is 10^5 N/mm^3. It is in the range of the proposed values by Turon et al. [32]. It is also found that the predicted load-POD curve is similar to that using a penalty stiffness value of 10^6 N/mm^3. The mass was scaled up by a factor of about 100,000 in the Hi-FEM model to reduce run times. Dynamic effects were checked by calculating the

ratio between the kinetic energy and the internal energy, which was sufficiently low that the results were not affected.

3. OCT experimental and Hi-FEM modelling results

Scaled-down OCT tests were conducted to verify the Hi-FEM. In the experiments, the specimens were connected to two steel arms through loading pins at the hole at each side as shown in Figure 1. The two steel arms were then connected to steel extension bars by pins at each side. The experiments were under displacement control at a rate of 0.5 mm/min. The POD was measured at the crossheads where the steel extension bars were clamped to the Instron hydraulic-driven universal test machine, with a load cell of 100 kN. No anti-buckling guides were used, and no buckling was observed in any of the tests. Three specimens were tested up to ultimate failure. Another 3 tests were stopped at different load levels. The 3 specimens taken from the interrupted tests were soaked in a bath of zinc iodide penetrant in preparation for CT scanning. A Nikon XT H 225ST CT scanner was used, which has a proprietary 225 kV microfocus X-ray source with a 3 μm voxel size.

The modelling results are shown in Figure 5. No filtering is applied to produce the curve from the analysis. At the beginning of the virtual OCT test, the predicted load-POD response is linear. From 5.5 kN onwards, some small load drops are predicted. As the load increases, larger load drops occur around the peak load at about 8.0 kN. Then the load starts to decrease as the POD increases, which is accompanied by further load drops. The model fails to run past about 1.4 mm POD due to severe element distortion. The Hi-FEM modelling results are also compared against the 3 scaled-down OCT test results in Figure 5. The predicted and measured load-POD curves are consistent in terms of the failure load envelope. The initial slope of the predicted load-POD curve is

steeper in the virtual test because the experimental POD was measured at the crosshead. Initially, the test fixture assembly had some compliance and stiffened up as the loading arms lined up. Therefore, the measured stiffness slightly increased at the beginning of the tests, and then stabilised. In the scaled-down OCT tests, at around 5.5 kN, some small load drops were observed, then some larger load drops near the peak loads at around 8.0 kN. These are well captured by the Hi-FEM model as shown in Figure 5. However, the magnitude of the predicted load drops is much smaller than those observed in the experiments. Finally, some major load drops occurred at around 1.4 mm POD on the let-down curve due to compressive failure at the rear end of the specimens. Compressive failure was not included in the current Hi-FEM model which is developed for Mode I tensile trans-laminar fracture, and so this phase of the test was not modelled.

4. FPZ development and fracture propagation

In the current study, the Mode I trans-laminar fracture response in the virtual OCT test can be divided into 4 stages as shown in Figure 6: (1) FPZ development – Cohesive interface elements representing the sub-critical damage including splitting and delamination fail at the notch tip at first. The deletion of continuum elements which represents fibre fracture then starts to occur in some 0° plies. This corresponds to the early small load drops on the predicted load-POD curve. (2) Initial fracture propagation – sub-critical damage and fibre fracture in the 0° plies have grown, and then the ±45° plies also break. To avoid any local mesh effects, the fibre breakage was checked to see when it grows beyond the very first unit cell in the ±45° plies at the notch tip. When this happens, the predicted FPZ development comes to an end because plies of all orientations are broken through the model thickness. (3) Stable fracture propagation – fibre fracture propagates, and the crack extends stably. The predicted load continues to

grow, and then falls. (4) Model termination – The Hi-FEM model coincidentally stops running at a similar load level to when compressive failure started in the experiments at the rear end of the specimens. The current Hi-FEM was not developed to predict the compressive failure seen in the experiments, because it is not relevant to the characterisation of Mode I trans-laminar fracture energy. The stable fracture propagation was closely simulated in the virtual OCT test before compressive failure occurs in the experiments. The present Hi-FEM helps to better understand the damage state and crack growth in detail throughout the virtual OCT test, which is hard to examine experimentally.

The FPZ development has already been predicted in the previous work [13]. To predict fracture propagation beyond the FPZ development, we need to understand how the crack length jumps unstably in increments. In the OCT tests, crack jumps were observed at the large load drops during fracture propagation. Since the 0° plies are already broken in the FPZ, the jumps could be explained as the sudden transformation of the FPZ into a crack increment by the fracture of the ±45° plies. A new FPZ is then formed at the new crack front. The crack jumps repeat in a stepwise manner throughout the OCT test as the newly formed FPZ at the new crack tip turns into another crack increment. This is consistent with the findings reported by Zobeiry et al. [10], in which they identified the sudden damage extensions by constructing the damage length-POD curve. The load drops in the Hi-FEM model are smaller than those in the scaled-down OCT tests as shown in Figure 6. This is because elements are deleted one at a time in the Hi-FEM model, whereas in the OCT tests a larger cluster of fibres fail in a single event. As a result, the predicted crack jumps are more gradual than experimentally observed. To capture the crack extension accurately, a critical volume of elements

would need to be removed at the same time.

To describe fracture propagation accurately, we also need to clearly define the crack length based on experimental observations [26]. There are two different definitions of crack lengths used here in the virtual OCT test and the experiments as shown in Figure 7. The true crack length a is defined as the distance over which plies of all orientations are broken. In principle, this should be all the plies, but in the present laminate, there is more delamination at the central double -45° ply. As a result, this ply fails much later but still loses traction due to the large delamination reaching the loading pin. The crack length is therefore defined as the distance over which all the other plies are broken. The crack length is therefore defined as the distance over which all the other plies are broken. In front of the crack is an FPZ where the 0° plies are broken but some ±45° plies are still intact. The combined true crack length plus the FPZ constitutes the effective crack length a_{eff}.

As shown in the Hi-FEM modelling results in Figure 6, the effective crack increments Δa_{eff} can be visualized from the loading-direction stress contours in a typical 0° ply. The extent of deleted continuum elements, and the position of stress concentrations along the crack path indicate the location of the new effective crack front. Three scaled-down OCT specimens from the interrupted tests were CT scanned to verify the Hi-FEM predicted crack increments. The 3 tests were stopped at the first large load drop (6.8 kN), after the peak load (7.6 kN) and just before the major load drop (7.2 kN) due to compressive failure, respectively. The load levels at which the stress contours were extracted in the virtual OCT tests (the corresponding predicted crack jumps) could not be matched exactly but are very similar: 6.9 kN (1 mm), 7.9 kN (4.5 mm) and 7.3 kN (6.5 mm) respectively. It can be seen in Figure 6 that the effective

crack increments Δa_{eff} are very well predicted.

The effective crack length a_{eff} is related to the true crack length a via the size of the FPZ. The size of the fully developed FPZ (l_{FPZ}) for IM7/8552 QI laminates has been measured in different tests with various specimen configurations and found to be similar. For example, l_{FPZ} = 2.3 mm (C.V. 7%) was previously measured from large centre-notched tensile tests, and l_{FPZ} = 2.6 mm (C.V. 18%) from previous scaled-down OCT tests. Although these results were for a slightly different $[45/90/-45/0]_{4s}$ layup, this is not expected to affect the size of the fully developed FPZ. It has already been demonstrated that the two different stacking sequences are comparable because they show similar Mode I trans-laminar fracture energy for initial fracture propagation [33]. Therefore, the average measured value of 2.5 mm can be used for the size of the fully developed FPZ. In the Hi-FEM model, when fibre failure is predicted to happen within the first unit cell at the notch tip in all ±45° plies except for the central double -45° ply, the predicted fibre breakage in the 0° plies is small and the predicted failure load is also low. This is due to the local mesh effect because the numerical notch tip is sharper than that in the coupons. But once the fibre breakage goes beyond the first unit cell into other unit cells in most of the ±45° plies, the simulated fibre breakage in the 0° plies which determines the size of the fully developed FPZ is the same as the measured average size of the fully developed FPZ (l_{FPZ} = 2.5 mm). Also, in the Hi-FEM model the overall extent of damage and fracture in all ±45° plies is hard to quantify numerically at each time increment throughout the analysis due to the complexity of the damage, and so the size of the FPZ is also hard to define. This is because the fibre breakage in the different +45° and -45° plies is not aligned with each other and with those in the 0° plies at each time step. The crack front in the ±45° plies also slightly deviates from the crack path in

the 0° plies, as it is influenced by the ±45° splitting. Hence, a constant size of the fully developed FPZ (l_{FPZ} = 2.5 mm) is used in the following analysis for simplicity.

5. R-curve determination

The Mode I trans-laminar fracture energy G_C (equal to R) was determined by the Numerical Compliance Calibration (NCC) method using Equation 2. All parameters for the G_C calculations are from the Hi-FEM analysis.

$$G_C = \frac{P^2}{2B}\frac{dC}{da_{eff}} \quad (2)$$

where P is the predicted force before the numerical load drop, a_{eff} is the predicted effective crack length after the numerical load drop based on the fibre breakage in the 0° plies, B is the nominal specimen thickness and C is the numerical compliance from the Hi-FEM predicted load-POD curve. Initially, the R-curve is based on the predicted effective crack length a_{eff}, which is consistent with the literature [4-6]. An adjustment to the R-curve will be discussed later based on the true crack length a.

The numerical compliance C = POD/P was calculated from the predicted force and POD. The predicted compliance C is drawn against the effective crack length a_{eff} and fitted by a polynomial function as shown in Figure 8, so its derivative dC/da_{eff} can be determined. The determined G_C values (equal to R) from the virtual OCT test are plotted against the effective crack increment Δa_{eff} to form the effective R-curve in Figure 9. The effective R-curve appears to be approaching a plateau, with a value of 143.5 kJ/m^2 before the Hi-FEM model stops running. Whether the R-curve has reached a plateau is not conclusive due to limited data, and larger specimens will be tested in the future to investigate this.

The height of the FPZ is also an important parameter. It can be quantified by the extent of delamination and splitting. The maximum height of the delaminated area at

each interface which is represented by the fully failed cohesive interface elements is averaged through the model thicknesses for different effective crack increments in Table 2. The damage height grows during the virtual OCT test, and its growth rate appears to slow down with increasing effective crack increments. The predicted maximum average damage height of 6.9 mm is similar to the previously reported value for steady-state fracture propagation for a slightly different $[45/90/-45/0]_{4s}$ layup [12]. In Ref. [12], the damage height was measured by Scanning Electron Microscopy (SEM) and DIC, and was found to grow and reach a steady-state value of 5 to 6 mm in the standard OCT tests where stable fracture propagation was observed.

In Figure 10, the damage height is also plotted against the effective crack increment. The shape of the damage height vs. effective crack increment curve is similar to the shape of the effective R-curve. This suggests that the growth of the damage height is responsible for the R-curve effect in the QI laminate, due to more energy being dissipated over a larger delamination area and longer splits that accompany the increasing damage height. Teixeira et al. [7] related the effect of increasing trans-laminar fracture toughness with ply thickness to the fibre pull-out length, which is a similar mechanism in a different cross-ply laminate.

6. Discussion

Here an alternative definition of the R-curve is proposed, by excluding the FPZ development in the crack length for the QI laminates. This is because before all the plies are broken (except for the central double -45° ply where more delamination is present), the FPZ is still developing and does not really constitute a crack. The determined trans-laminar fracture energy values before the FPZ is fully developed are therefore not really appropriate to be regarded as a part of the true R-curve. Only after all plies are broken in

the current QI laminate except for the central double -45° ply, does the initial crack start to grow, and the determined trans-laminar fracture energy values form the true R-curve. It is thus proposed to define the true crack length as the distance over which all plies are broken except for the central double -45° ply where more delamination is present, i.e. the effective crack length a_{eff} less the size of the FPZ. Here, the size of the fully developed FPZ (l_{FPZ} = 2.5 mm) is used for the determination of the true R-curve, which is the experimentally measured average value from Ref. [20, 26]. The intention of using this constant value is to simplify the crack length determination, as it is hard to put a precise value on the size of the FPZ throughout the simulation. Consequently, the effective R-curve in Figure 9 is shifted by l_{FPZ} = 2.5 mm to form the true R-curve in Figure 11. It was found in the current study that even after the FPZ is fully developed, the trans-laminar fracture energy continues to increase, which contributes to the true R-curve. In contrast, Bergan et al. [6] defined their "FPZ" differently as "an ambiguous measure for damage propagation". After their "FPZ" reaches a constant length, the trans-laminar fracture was assumed to reach a steady state.

The true R-curve determined using Hi-FEM is compared with the available *G*c values for 4 mm thick quasi-isotropic IM7/8552 laminates reported in literature. The trans-laminar fracture energy values for the same $[90/45/0/-45]_{4s}$ IM7/8552 laminates from Ref. [34] are shown in Figure 11. The Mode I trans-laminar fracture energy values were determined from two standard OCT tests using the area method. The crack increment was determined by post-processing the DIC data which defines the boundary of the FPZ [34]. This means that the crack increments in Ref. [34] are equivalent to the current effective crack increments. The crack increments in Ref. [34] have therefore been adjusted by subtracting l_{FPZ} = 2.5 mm to compare to the current results for

consistency, except that the first point from Ref. [34] is set to correspond to "zero crack length" here to avoid any non-physical small negative true crack length. Only the results from Ref. [34] over a comparable crack growth of 4.1 mm have been plotted in Figure 11. These vary from 90.5 to 123.6 kJ/m^2 over a 5 mm crack growth. This shows a similar trend to that currently predicted, but with more conservative values. The true R-curve is also compared against the Mode I trans-laminar fracture energy values for a slightly different IM7/8552 $[45/90/-45/0]_{4s}$ laminate which has been shown to behave similarly during initial fracture propagation [33]. In Figure 11, the starting point of the true R-curve at 92.0 kJ/m^2 is similar to 93 kJ/m^2 (C.V. 5.8%) which is the value measured from the largest IM7/8552 $[45/90/-45/0]_{4s}$ centre-notched tensile tests in Xu et al. [20] where the specimen size is large enough to have a fully developed FPZ. Another reported value of 69 kJ/m^2 (C.V. 8.7%) for the initial fracture propagation derived directly from the previous IM7/8552 $[45/90/-45/0]_{4s}$ scaled-down OCT tests is lower [26]. But this value was calculated using the ASTM E399 standard [23], which has been found to yield lower fracture energy values than the compliance calibration method according to Ref. [3]. It has also been reported that Mode I trans-laminar fracture energy varies from 90 to 115 kJ/m^2 from the IM7/8552 $[45/90/-45/0]_{4s}$ standard OCT tests with different notch radii, but no R-curves were included in Ref. [12]. To sum up, the predicted true R-curve is reasonably consistent with the range of reported values. In contrast, the starting point of the initially determined effective R-curve based on the effective crack length at 19.2 kJ/m^2 is much too low compared with the Mode I trans-laminar fracture energy values reported in the literature.

Whether R-curves start from zero or not is debatable. For example, the R-curves defined here and those in [4, 5, 7] do not start from zero, but the R-curve defined in Ref.

[6] does start from zero. It depends on how the crack length is defined. Based on our definition of effective crack length (including the FPZ), only after some fibres in the 0° plies break does the effective R-curve start. Based on our alternative definition of the true crack length (excluding the FPZ), the whole laminate including the 0° and ±45° plies needs to break or delaminate to form an open crack. In addition, a stress singularity does not exist in a real laminate due to the stress blunting effect of the 0° splitting. With the presence of 0° splitting, fibre fracture is delayed, so the R-curves based on our crack length definitions do not start from zero.

It has previously been demonstrated that the R-curve depends on the stacking sequence in cross-ply laminates [35]. The fracture propagation in QI laminates is also affected by different stacking sequences with or without central double 0° plies [33]. Hi-FEM can be used to predict R-curves with different stacking sequences and will be addressed in future work.

7. Conclusions and future work

The Mode I trans-laminar fracture behaviour was successfully predicted using a High-fidelity Finite Element Method (Hi-FEM), including the increasing load and damage height during crack growth. An effective R-curve was determined for IM7/8552 carbon/epoxy Quasi-isotropic (QI) laminates, by using the Numerical Compliance Calibration (NCC) method and the effective crack lengths which include the Fracture Process Zone (FPZ). The input parameters were mainly from independent characterisation tests.

A distinction is also discussed between the true crack length and the effective crack length. In the experiments, only after all the plies are broken (except for the centre double -45° ply where more delamination is present), can a full crack be considered to

propagate and the true R-curve start. The predicted effective R-curve is therefore adjusted by shifting by the size of the fully developed FPZ (l_{FPZ} = 2.5 mm) to form the true R-curve. The predicted true R-curve for Mode I trans-laminar fracture of the IM7/8552 carbon/epoxy $[90/45/0/-45]_{4s}$ laminate starts from 92.0 kJ/m^2, rising to 143.5 kJ/m^2, which is generally consistent with the range of values for 4 mm-thick QI IM7/8552 laminates reported in the literature. It was also found that the growth of the damage height during fracture propagation correlates with the increasing trans-laminar fracture energy and it is hypothesised that this may be the cause of the R-curve effect.

The current Hi-FEM can be used as a virtual test to determine fracture properties such as damage heights and R-curves and help to better understand Mode I trans-laminar fracture toughness testing. In the future, the Hi-FEM could be used to provide input values for global finite element models, based only on fundamental material properties from independent tests.

References

[1] Broek D. Elementary engineering fracture mechanics. Fourth revised ed. London: Kluwer Academic Publishers; 1986.

[2] Pinho ST, Robinson P, Iannucci L. Fracture toughness of the tensile and compressive fibre failure modes in laminated composites. Composites Science and Technology. 2006;66(13):2069-79.

[3] Laffan MJ, Pinho ST, Robinson P, Iannucci L. Measurement of the in situ ply fracture toughness associated with mode I fibre tensile failure in FRP. Part I: Data reduction. Composites Science and Technology. 2010;70(4):606-13.

[4] Catalanotti G, Camanho PP, Xavier J, Dávila CG, Marques AT. Measurement of resistance curves in the longitudinal failure of composites using digital image correlation. Composites Science and Technology. 2010;70(13):1986-93.

[5] Camanho PP, Catalanotti G. On the relation between the mode I fracture toughness of a composite laminate and that of a 0° ply: Analytical model and experimental validation. Engineering Fracture Mechanics. 2011;78(13):2535-46.

[6] Bergan A, Dávila C, Leone F, Awerbuch J, Tan T-M. A Mode I cohesive law characterization procedure for through-the-thickness crack propagation in composite laminates. Composites Part B: Engineering. 2016;94:338-49.

[7] Teixeira RF, Pinho ST, Robinson P. Thickness-dependence of the translaminar fracture toughness: Experimental study using thin-ply composites. Composites Part A: Applied Science and Manufacturing. 2016;90:33-44.

[8] Xu X, Takeda S, Aoki Y, Hallett SR, Wisnom MR. Predicting notched tensile strength of full-scale composite structures from small coupons using fracture mechanics. Composite Structures. 2017;180:386-94.

[9] Maimí P, González EV, Gascons N, Ripoll L. Size effect law and critical distance theories to predict the nominal strength of quasibrittle structures. Applied Mechanics Reviews. 2013;65(2):020803--16.

[10] Zobeiry N, Vaziri R, Poursartip A. Characterization of strain-softening behavior and failure mechanisms of composites under tension and compression. Composites Part A: Applied Science and Manufacturing. 2015;68(0):29-41.

[11] Ortega A, Maimí P, González EV, Trias D. Characterization of the translaminar fracture Cohesive Law. Composites Part A: Applied Science and Manufacturing. 2016;91:501-9.

[12] Zobeiry N, Forghani A, McGregor C, McClennan S, Vaziri R, Poursartip A. Effective calibration and validation of a nonlocal continuum damage model for laminated composites. Composite Structures. 2017;173:188-95.

[13] Xu X, Wisnom MR, Li X, Hallett SR. A numerical investigation into size effects in centre-notched quasi-isotropic carbon/epoxy laminates. Composites Science and Technology. 2015;111(0):32-9.

[14] Xu X, Paul A, Wisnom MR. Thickness effect on Mode I trans-laminar fracture toughness of quasi-isotropic carbon/epoxy laminates. Composite Structures. 2019;210:145-51.

[15] van der Meer FP, Sluys LJ, Hallett SR, Wisnom MR. Computational modeling of complex failure mechanisms in laminates. J Compos Mater. 2011;46(5):603-23.

[16] Mollenhauer D, Ward L, Iarve E, Putthanarat S, Hoos K, Hallett S, Li X. Simulation of discrete damage in composite Overheight Compact Tension specimens. Composites Part A: Applied Science and Manufacturing. 2012;43(10):1667-79.

[17] Li X, Hallett SR, Wisnom MR. Numerical investigation of progressive damage and the effect of layup in overheight compact tension tests. Composites Part A: Applied Science and Manufacturing. 2012;43(11):2137-50.

[18] Catalanotti G, Arteiro A, Hayati M, Camanho PP. Determination of the mode I crack resistance curve of polymer composites using the size-effect law. Engineering Fracture Mechanics. 2013;118:49-65.

[19] Laffan MJ, Pinho ST, Robinson P, McMillan AJ. Translaminar fracture toughness testing of composites: A review. Polymer Testing. 2012;31(3):481-9.

[20] Xu X, Wisnom MR, Mahadik Y, Hallett SR. An experimental investigation into size effects in quasi-isotropic carbon/epoxy laminates with sharp and blunt notches. Composites Science and Technology. 2014;100(0):220-7.

[21] Bažant ZP, Daniel IM, Li ZZ. Size effect and fracture characteristics of composite laminates. J Eng Mater Technol-Trans ASME. 1996;118(3):317-24.

[22] Salviato M, Kirane K, Esna Ashari S, Bažant ZP, Cusatis G. Experimental and numerical investigation of intra-laminar energy dissipation and size effect in two-dimensional textile composites. Composites Science and Technology. 2016;135:67-75.

[23] ASTM, Standard, E399-90. Standard test method for plane-strain fracture toughness of metallic materials. West Conshohocken, PA, USA: ASTM International; 1990 (1997).

[24] Kongshavn I, Poursartip A. Experimental investigation of a strain-softening approach to predicting failure in notched fibre-reinforced composite laminates. Composites Science and Technology. 1999;59(1):29-40.

[25] Li X, Hallett SR, Wisnom MR, Zobeiry N, Vaziri R, Poursartip A. Experimental study of damage propagation in Over-height Compact Tension tests. Composites Part A: Applied Science and Manufacturing. 2009;40(12):1891-9.

[26] Xu X, Wisnom MR, Mahadik Y, Hallett SR. Scaling of fracture response in over-height compact tension tests. Composites Part A: Applied Science and Manufacturing. 2015;69(0):40-8.

[27] Daniel IM. Strain and failure analysis of graphite/epoxy plates with cracks. Exp Mech. 1978;18(7):246-52.

[28] Li X, Hallett Stephen R, Wisnom Michael R. Modelling the effect of gaps and overlaps in automated fibre placement (AFP)-manufactured laminates. Science and Engineering of Composite Materials. 2015;22:115-29.

[29] Jiang W-G, Hallett SR, Green BG, Wisnom MR. A concise interface constitutive law for analysis of delamination and splitting in composite materials and its application to scaled notched tensile specimens. International Journal for Numerical Methods in Engineering. 2007;69(9):1982-95.

[30] Weibull W. A statistical distribution function of wide applicability. Journal of Applied Mechanics. 1951;18:293-7.

[31] Hallett SR, Green BG, Jiang W-G, Wisnom MR. An experimental and numerical investigation into the damage mechanisms in notched composites. Composites Part A: Applied Science and Manufacturing. 2009;40(5):613-24.

[32] Turon A, Dávila CG, Camanho PP, Costa J. An engineering solution for mesh size effects in the simulation of delamination using cohesive zone models. Engineering Fracture Mechanics. 2007;74(10):1665-82.

[33] Xu X, Wisnom MR, Hallett SR, Zobeiry N, Leslie S, Poursartip A, Vaziri R. Stacking sequence effects in over-height compact tension tests of quasi-isotropic laminates. 19th International Conference on Composite Materials. Montreal, 2013.

[34] Zobeiry N. Extracting the strain-softening response of composites using full-field displacement measurement. Vancouver: PhD Thesis, The University of British Columbia; 2010.

[35] Laffan MJ, Pinho ST, Robinson P, Iannucci L. Measurement of the in situ ply fracture toughness associated with mode I fibre tensile failure in FRP. Part II: Size and lay-up effects. Composites Science and Technology. 2010;70(4):614-21.

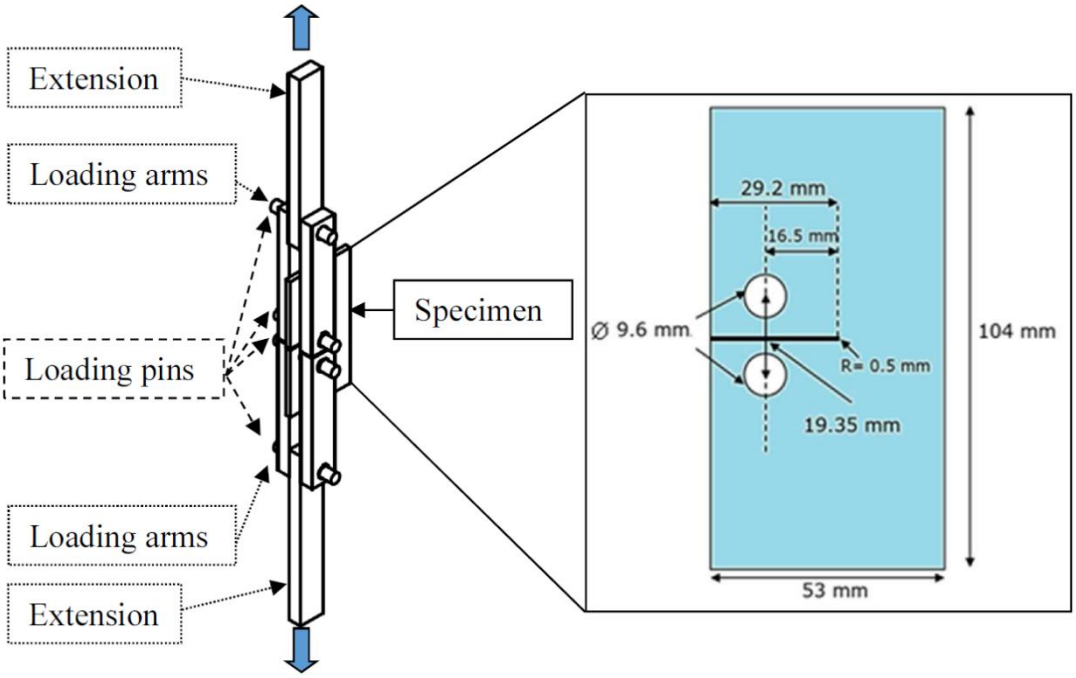

Figure 1. Scaled-down OCT specimen modelled and test fixture.

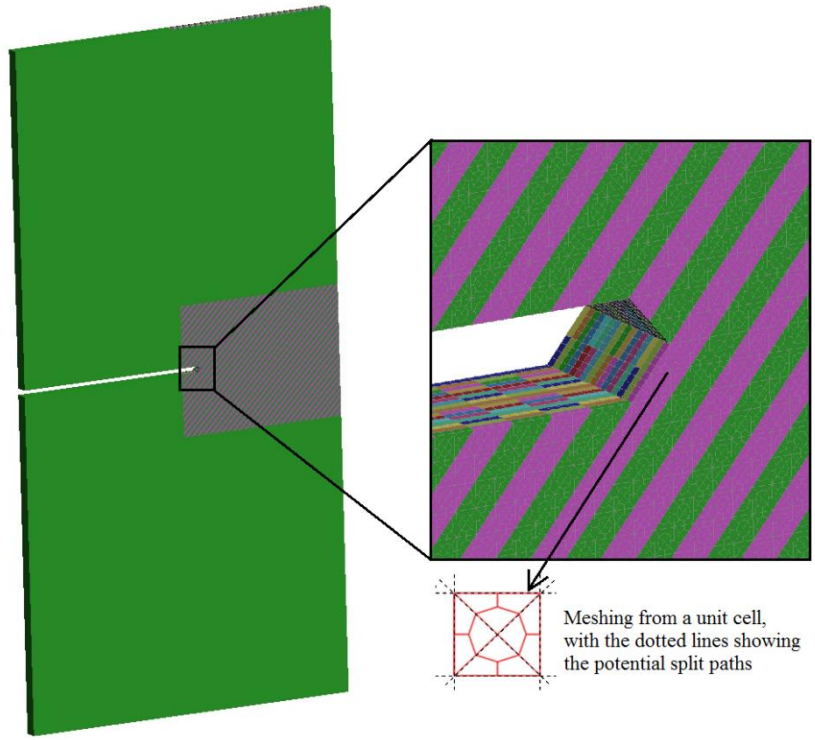

Figure 2. The mesh detail at the notch tip in the Hi-FEM model (different colours are for parts between which cohesive interface elements are inserted).

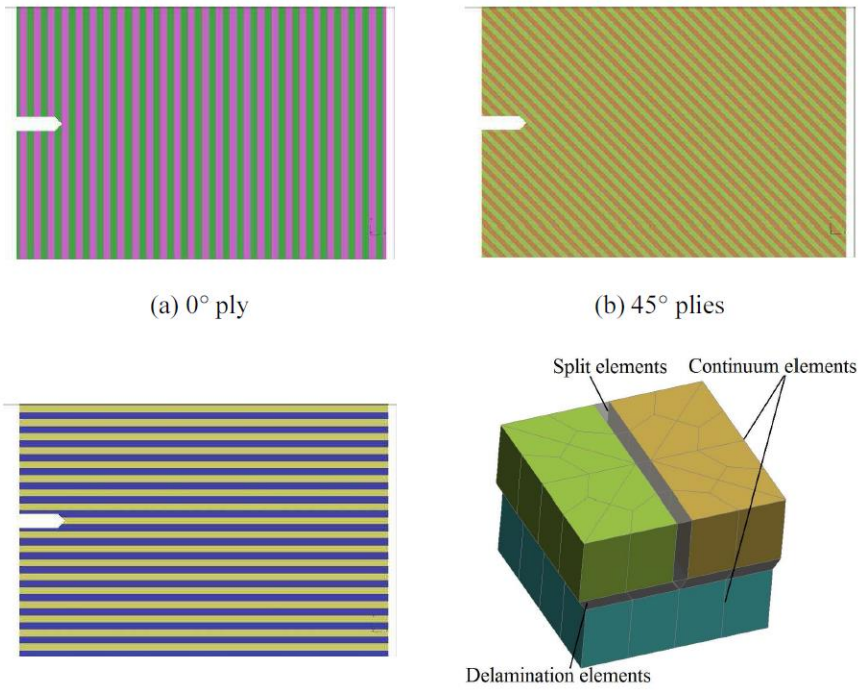

Figure 3. Potential split paths in the Hi-FEM model and element connectivity (different colours for different parts between which split elements are inserted).

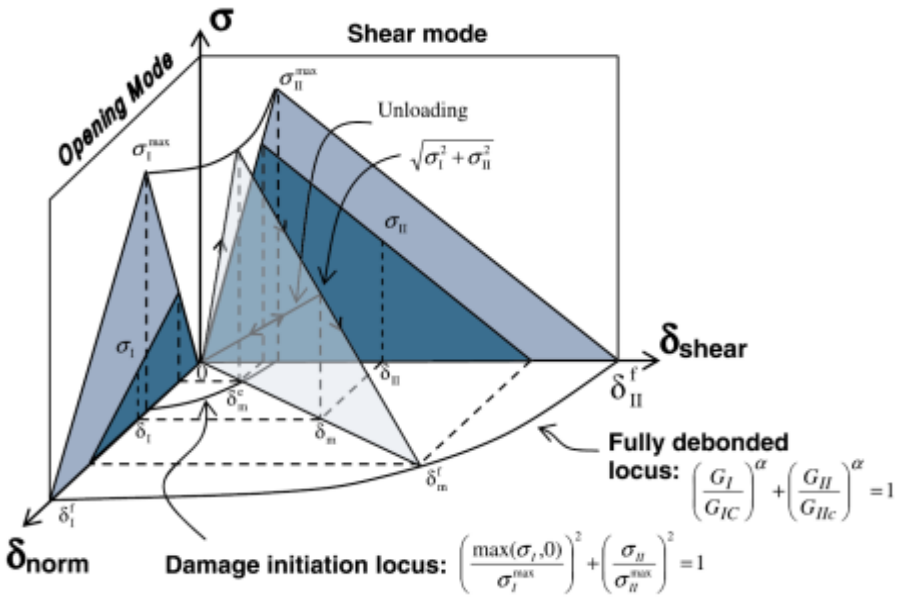

Figure 4. Illustration of the mixed-mode traction-displacement relationship used in the cohesive interface element formulation of Ref. [29].

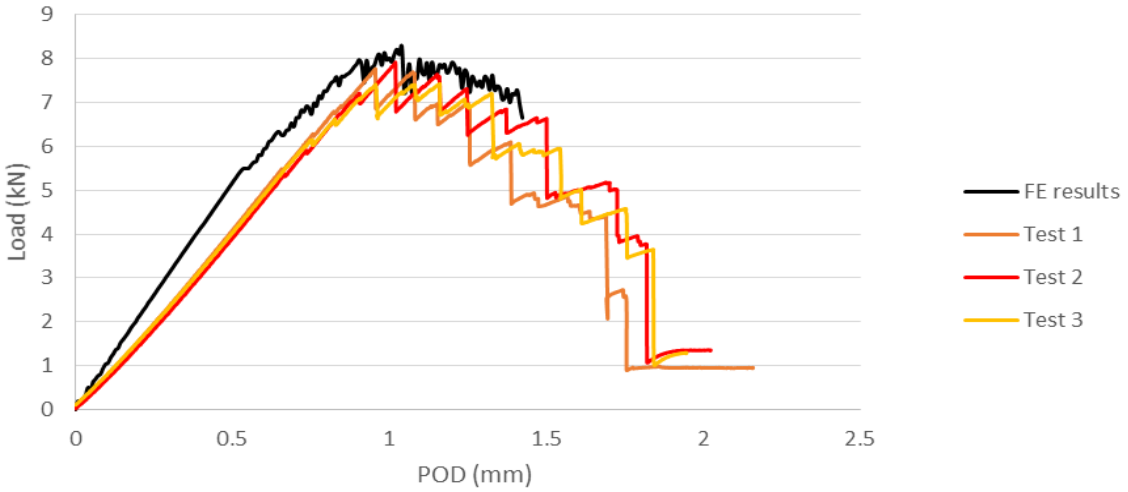

Figure 5. Hi-FEM modelling vs. experimental results.

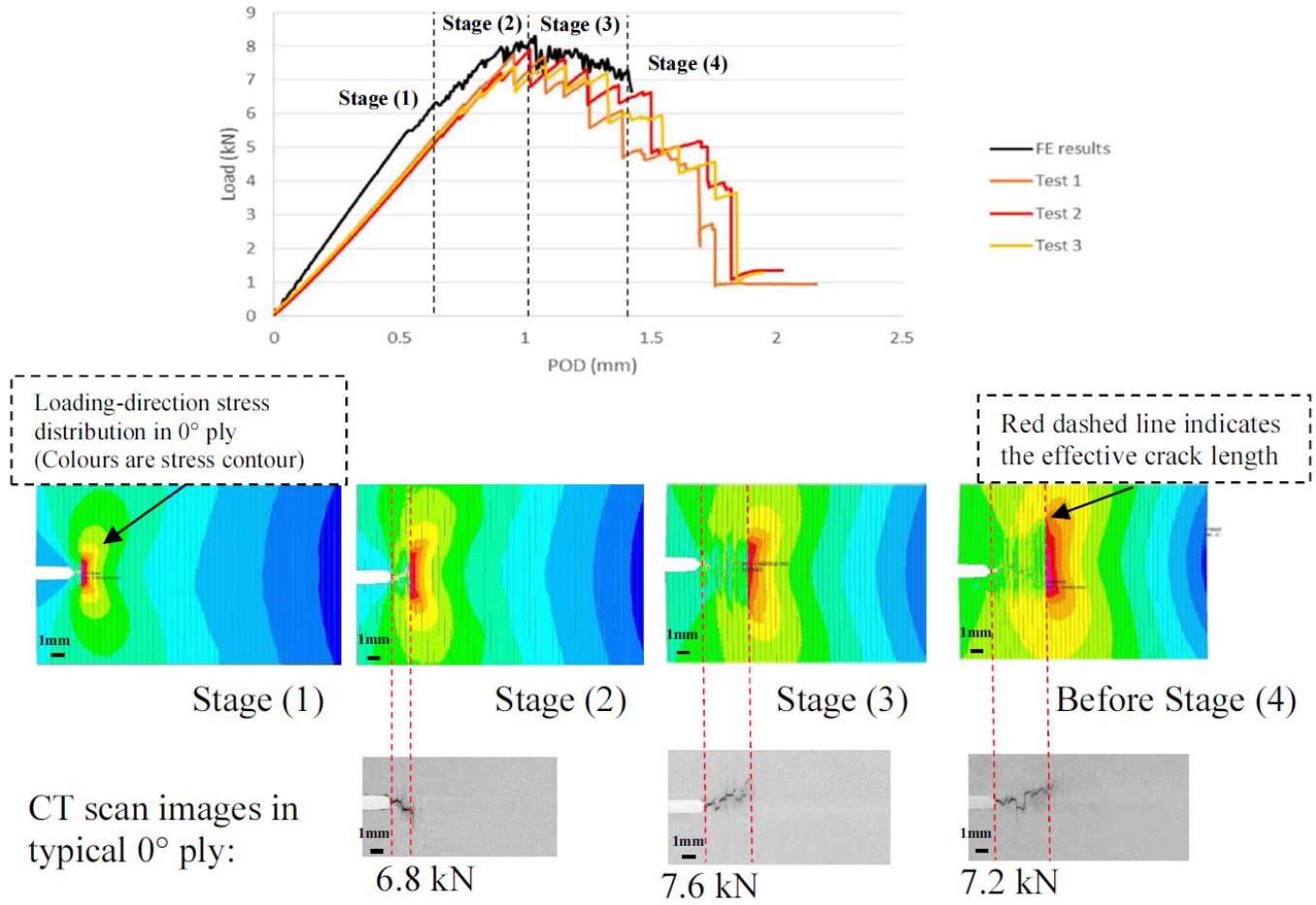

Figure 6. Fibre breakage and stress contours in typical 0° plies in 4 stages compared to the CT scan images (the notch width is 1 mm in all images): (1) FPZ development; (2) Initial fracture propagation; (3) Stable fracture propagation (4) Model termination.

Hi-FEM with predicted fibre fracture in red	CT images with observed crack in black

(a) Typical 0° ply

(b) Typical 45° ply

(c) Typical -45° ply

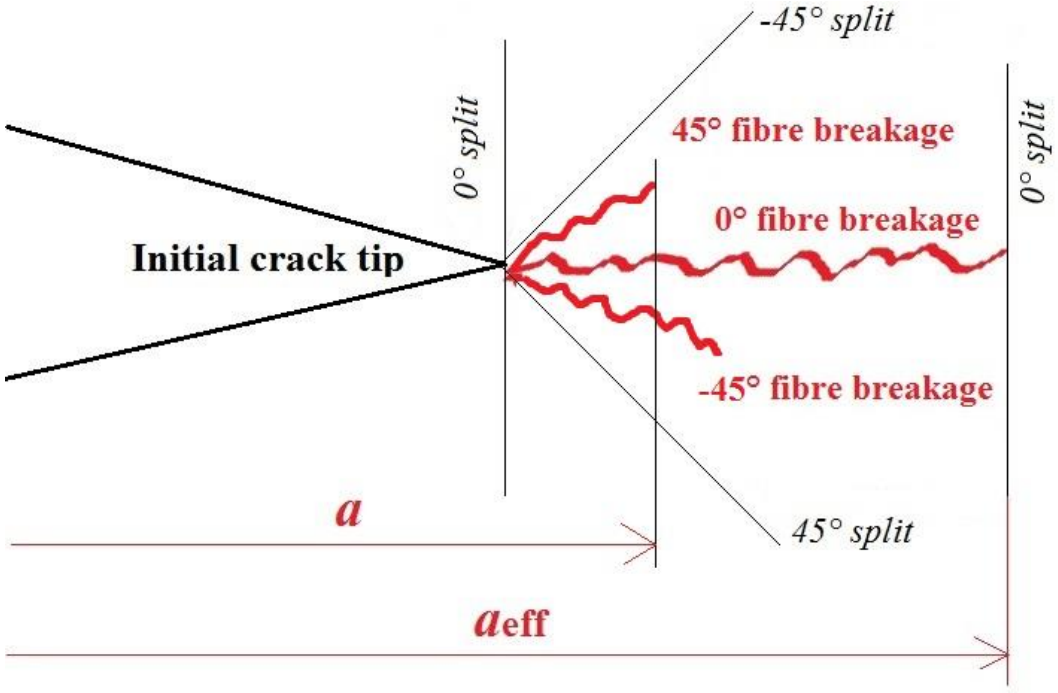

(d) Schematics

Figure 7. Two different definitions of crack lengths a_{eff} vs. a (same scale for (a)(b)(c)).

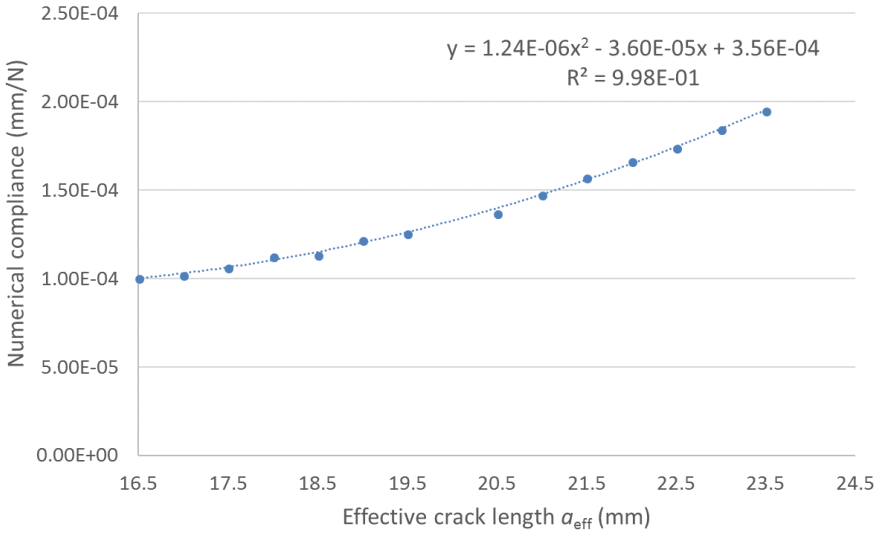

Figure 8. Numerical compliance from the Hi-FEM analysis.

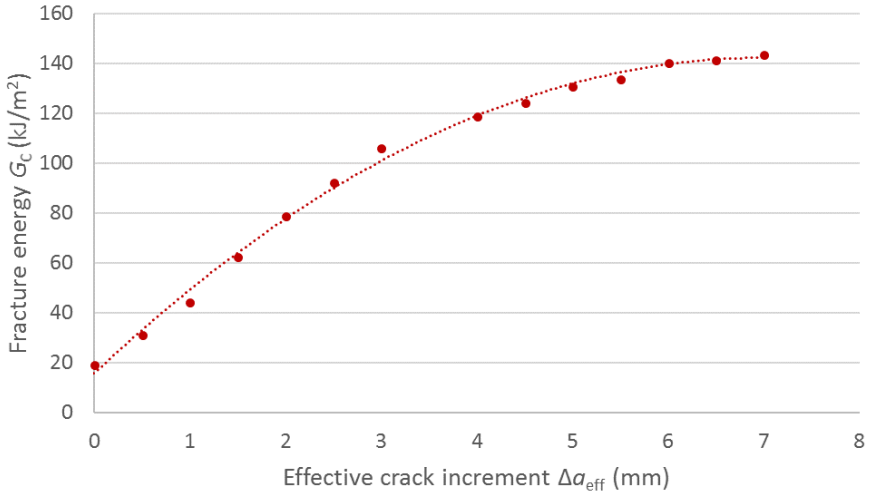

Figure 9. The predicted effective R-curve based on effective crack increments from the Hi-FEM analysis.

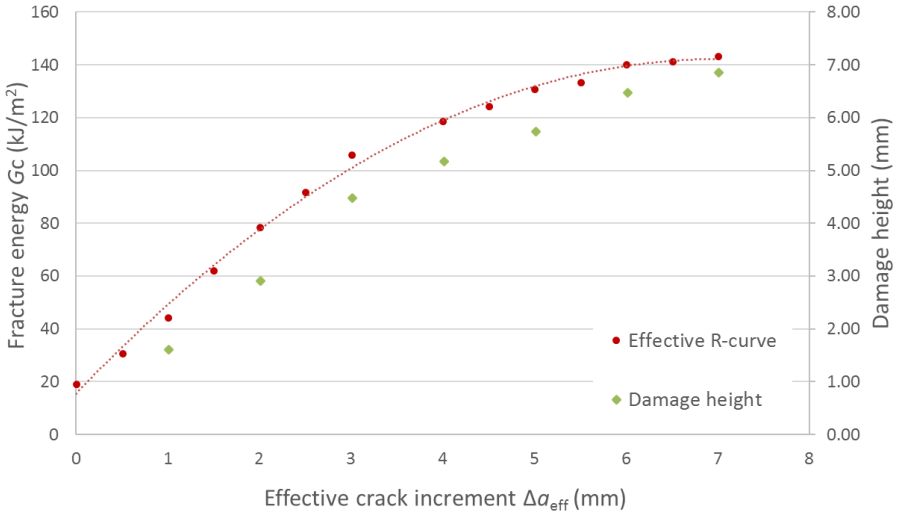

Figure 10. Growth of damage height causing the R-curve effect.

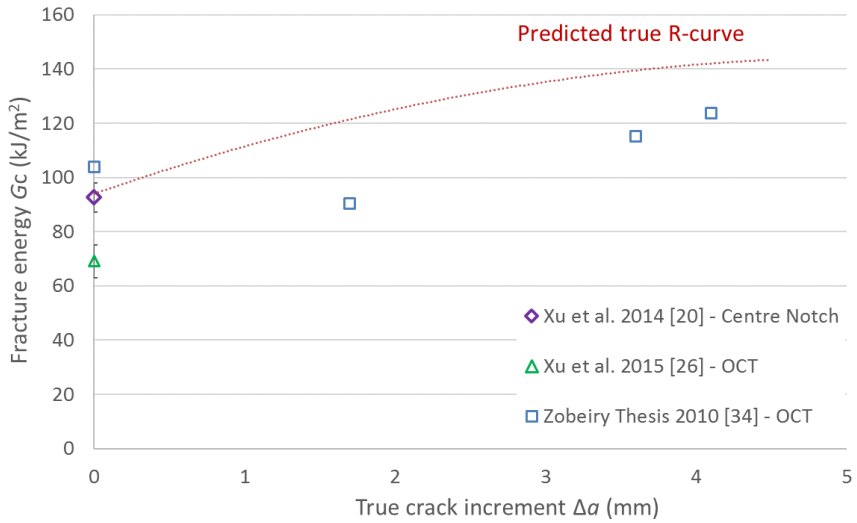

Figure 11. The predicted true R-curve based on true crack increments from the Hi-FEM analysis.

Table 1. Input parameters for the Hi-FEM model.

Properties of cohesive interface elements				
G_{IC} (N/mm)	G_{IIC} (N/mm)	σ_I^{max} (MPa)	σ_{II}^{max} (MPa)	α
0.2	1.0	60	90	1
Properties of continuum elements				
E_{11} (GPa)	E_{22}=E_{33} (GPa)	G_{12}=G_{13} (GPa)	G_{23} (GPa)	m
161	11.4	5.17	3.98	41
σ_{unit} (MPa)	α_{22}= α_{33} ($^oC^{-1}$)	α_{11} ($^oC^{-1}$)	υ_{12}=υ_{13}	υ_{23}
3131[1]	3×10^{-5}	0.0	0.320	0.436

[1] 3131 MPa is for a unit volume of material.

Table 2. Growth of predicted damage height during the virtual OCT test (mm).

Effective crack increment	1	2	3	4	5	6	7
Average damage height	1.63	2.94	4.50	5.20	5.77	6.49	6.89